On the relation between basal erosion of the lithosphere and surface heat flux for continental plume tracks

Björn H. Heyn[1] and Clinton P. Conrad[1]

[1]Centre for Earth Evolution and Dynamics

November 24, 2022

Abstract

While hotspot tracks beneath thin oceanic lithosphere are visible as volcanic island chains, the plume-lithosphere interaction for thick continental or cratonic lithosphere often remains hidden due to the lack of volcanism. To identify plume tracks with missing volcanism, we characterize the amplitude and timing of surface heat flux anomalies following a plume-lithosphere interaction using mantle convection models. Our numerical results confirm an analytical relationship in which surface heat flux increases with the extent of lithosphere thinning, which is primarily controlled by on the viscosity structure of the lower lithosphere and the asthenosphere. We find that lithosphere thinning is greatest when the plate is above the plume conduit, while the maximum heat flux anomaly occurs about 40-140\,Myr later. Therefore, younger continental and cratonic plume tracks can be identified by observed lithosphere thinning, and older tracks by an increased surface heat flux, even if they lack extrusive magmatism.

On the relation between basal erosion of the lithosphere and surface heat flux for continental plume tracks

Björn H. Heyn [1], Clinton P. Conrad [1]

[1]Centre for Earth Evolution and Dynamics (CEED), University of Oslo, Norway

Key Points:

- We used numerical and analytical approaches to characterize heat flux anomalies following plume impingement on the lithosphere
- Surface heat flux anomalies follow an analytical relationship that predicts increasing heat flux with increasing basal lithospheric erosion
- Lithosphere thinning is mostly controlled by viscosity structure, with a maximum surface heat flux anomaly following 40-140 Myr later

Corresponding author: Björn H. Heyn, `b.h.heyn@geo.uio.no`

Abstract

While hotspot tracks beneath thin oceanic lithosphere are visible as volcanic island chains, the plume-lithosphere interaction for thick continental or cratonic lithosphere often remains hidden due to the lack of volcanism. To identify plume tracks with missing volcanism, we characterize the amplitude and timing of surface heat flux anomalies following a plume-lithosphere interaction using mantle convection models. Our numerical results confirm an analytical relationship in which surface heat flux increases with the extent of lithosphere thinning, which is primarily controlled by on the viscosity structure of the lower lithosphere and the asthenosphere. We find that lithosphere thinning is greatest when the plate is above the plume conduit, while the maximum heat flux anomaly occurs about 40-140 Myr later. Therefore, younger continental and cratonic plume tracks can be identified by observed lithosphere thinning, and older tracks by an increased surface heat flux, even if they lack extrusive magmatism.

Plain Language Summary

Extra heat is transmitted through Earth's tectonic plates above hot upwellings called plumes, and contributes to the heat budget of glaciated regions such as Greenland. A thin oceanic plate moving over such an upwelling typically yields a chain of age-progressing volcanic islands such as Hawaii. However, such volcanism is often missing in continental regions such as Africa or Greenland, which have thicker plates. Nonetheless, the passage of the plate over the upwelling leaves a trace in form a reduced plate thickness and an increased amount of emitted heat even millions of years after the plume passage. In this study, we use numerical models of mantle convection to show that these two observations are directly linked to each other, with a larger heat flux anomaly observed for areas that have been thinned more. Furthermore, we demonstrate that there is a significant time delay between the thinning, which happens during the passage of the upwelling, and the heat flux that is observed many millions of years later. As a consequence, past interactions of plates with plumes can influence today's heat output in continental regions.

1 Introduction

One of the most prominent surface expressions of mantle convection is linked to the interaction of deep-rooted mantle upwellings, so-called plumes, with the lithosphere.

The arrival of plume heads is thought to cause massive volcanism in the form of large igneous provinces (LIPs) (e.g. Richards et al., 1989; Torsvik et al., 2016), which are found on both continents and seafloor. For relatively thin oceanic plates, hotspot tracks of volcanic islands delineate the path of the plate over the plume tail (e.g. Morgan, 1971; Harrison et al., 2017; Dannberg & Gassmöller, 2018). These plume tracks can be used link LIPs with current-day hotspot volcanism, and provide important information for the reconstruction of plate motions (Doubrovine et al., 2012; Bono et al., 2019). However, these hotspot tracks of continuous extrusive volcanism are often missing on thicker continental lithosphere (Davies, 1994; Yang & Leng, 2014).

Oceanic hotspots and hotspot tracks have been analysed wth respect to several key properties, including their surface swell (King & Adam, 2014), lithosphere thinning (Ballmer et al., 2011) and geochemical composition and evolution of the erupted magmas (Huang et al., 2011; Harrison et al., 2017; Dannberg & Gassmöller, 2018). In contrast, investigations of continental plume-lithosphere interaction have been limited because it is difficult to identify continental hotspot tracks. For the North China craton (Polat et al., 2006; Wang et al., 2015), the cratons in Africa (e.g. Hansen et al., 2012; Hui et al., 2015; Koptev et al., 2016; Chang et al., 2020; Celli et al., 2020) and the Yellowstone hotspot (e.g. Shervais & Hanan, 2008; Yuan et al., 2010; Jean et al., 2014; Knott et al., 2020), most studies focus on the magmatic component of plume-lithosphere interaction, while Celli et al. (2020) focus on plume-induced destruction of cratonic roots. The erosion of lithosphere has also been studied for the Slave Craton (Liu et al., 2021), the Indian Craton (Sharma et al., 2018; Paul & Ghosh, 2021) and a hidden hotspot track in the eastern United States (Chu et al., 2013; Yang & Leng, 2014). All of these studies agree that plumes erode the the lithosphere, but it is still unclear whether the cratonic root can heal (as suggested for the Slave craton, Liu et al., 2021) or if the destruction is irreversible (as seen in Africa, Celli et al., 2020). Furthermore, the tectonic setting and age differ significantly between the examples given above, making it impossible to identfy systematic trends in the amount of lithospheric thinning associated with plume-lithosphere interaction.

Finally, there are two examples of plume-craton interaction for which extensive focus has been placed on heat flux: Marie Byrd Land in Antarctica (Seroussi et al., 2017; Shen et al., 2020; Lösing et al., 2020), and the Iceland plume in Greenland (e.g. Martos et al., 2018; Colgan et al., 2021). In both locations, the heat flux associated with the plume can have significant effects on the melting rates of ice (Rogozhina et al., 2016; Rysgaard et al., 2018; Smith-Johnsen et al., 2020). However, these two scenarios are quite different: while Antarctica has been rather stagnant over the plume (Seroussi et al., 2017), Greenland passed over the plume within about 30-90 Myr (for an overview of potential hotspot tracks, see Martos et al., 2018). For Greenland, seismic studies also suggest a thinned area above the plume track (e.g. Mordret, 2018; Celli et al., 2021), although the reported anomalies for heat flux, lithospheric thinning and reconstrcuted plume tracks vary significantly between different studies and often do not coincide. Therefore, a discrimination between the different scenarios requires a better and more systematic understanding of the interaction between plumes and cratonic lithosphere, and the effect of this interaction on geophysical observables. In this study, we use numerical and analytical approaches to characterize rhe relationship between surface heat flux and lithospheric thinning.

2 Model setup

We use 2-D and 3-D numerical models of mantle convection in Cartesian geometry to systematically investigate the connection between surface heat flux and lithosphere thinning. Modeling is done with the open source finite element code ASPECT (Heister et al., 2017; Kronbichler et al., 2012; Bangerth et al., 2020), and we use boxes of 1200 km by 600 km or 5500 km by 800 km (x by z dimensions, 5500 km by 2000 km by 800 km for 3-D) for stagnant and moving plate models, respectively. We define the initial temperature field as a linear gradient from the surface to the lithsophere-asthenosphere boundary represented by the 1500 K (or in some models the 1623 K) isotherm at a chosen depth, underlain by an upper mantle with a temperature gradient of about $1K/km$ and a temperature perturbation added at the base to generate a plume. For cases with stagnant plates, all domain sides are free-slip, except for the surface which is set to no-slip, and plume sources are removed after 50, 100, or 200 Myr. We obtain cases with moving plates by imposing a velocity component parallel to the x-axis on the top and uppermost (i.e. lithospheric) side walls, and a velocity that decreases linearly through the asthenosphere to a free-slip (no influx) condition below the base of the asthenosphere. All the remaining sides are set to free-slip. We neglect compressibilty and depth dependence of parameters (except for viscosity), as we expect their impact to be negligible for the purpose of this study (Albers & Christensen, 1996).

Viscosity is implemented via a modified diffusion-dislocation creep law with

$$\eta_{\text{eff}} = \frac{\eta_j}{\eta_{\text{ref}}} \left(\frac{1}{\eta_{\text{eff}}^{\text{diff}}} + \frac{1}{\eta_{\text{eff}}^{\text{disl}}} \right)^{-1}, \text{with} \tag{1}$$

$$\eta_{\text{eff}}^i = \frac{1}{2} A^{-\frac{1}{n_i}} d^{\frac{m_i}{n_i}} \dot{\epsilon}_i^{\frac{1-n_i}{n_i}} exp\left(\frac{E_i + PV_i}{n_i RT} \right). \tag{2}$$

Parameters in the equation above are the layer viscosity scaling η_j (implementing a viscosity jump beneath the asthenosphere), the reference viscosity η_{ref}, the prefactor A, the grain size d with the grain size exponent m, the strain rate $\dot{\epsilon}$ with the stress exponent n, the activation energy E and volume V, the gas constant R, pressure P and temperature T. The subscript i refers to either diffusion or dislocation creep. Depending on the choice of parameters, the resulting viscosity can be simplified to a Newtonian ($n = 1$) and grain size independent ($m = 0$) viscosity, as we choose in most of our simulations. In these models, we further simplify the equation by setting $V = 0$, making the viscosity only temperature-dependent. A change of viscosity with depth is then added as a stepwise viscosity increase below the asthenosphere via η_j. This means that we can control the temperature-dependence of viscosity via the activation energy, resulting in a viscosity increase with decreasing temperature. In some models, we employ a higher initial temperature for the lithosphere-asthenosphere boundary to decrease the lower lithosphere viscosity. All input parameters for the viscosity law are defined in Table S1 in the Supporting Information.

Our setup gives us direct control over several parameters that may affect the heat flux and lithosphere thinning: lithosphere thickness and viscosity, asthenosphere thickness and viscosity, plume excess temperature and the interaction time between the plume and the lithosphere (via plume lifetime or plate velocuty). In order to quantify their impact on the predicted heat flux and lithosphere thinning anomalies, we test a wide range of parameter combinations (see Tables S2-S4 in the Supporting Infromation), with the ranges given in Table S1. Due to computational costs, only parameters that are shown to be important in 2-D have been tested in 3-D geometry.

To quantify the effect of the plume on both lithospheric thickness and surface heat flux, we measure these plume-generated anomalies for every model relative to their average values over the first 300 km of x-direction (upstream of the plume) for each time step, which ideally represents a plume-unaffected lithosphere. This choice of reference value makes our results more easily comparable to heat flux and lithospheric structure observations since we only require information from one snapshot in time. However, the reference can be affected significantly by perturbations within the reference area, such as dripping instabilities that may temporarily appear to thicken the reference lithosphere, and thus cause an apparent increase in lithosphere thinning. We therefore use a relatively cool 1400 K isotherm as a reference for our calculation of the lithosphere thinning, as this isotherm is less affected by drip formation than the actual LAB. Finally, since the reference values for both heat flux and lithosphere vary within and between models, we express these anomalies as a percent of the reference value. For stagnant plate cases, we only track the evolution of the central maximum above the plume, while for moving plate cases, we track the overall maximum in time and space as well as the anomaly values at positions fixed in space (i.e. fixed x-positions) and fixed to the plate (i.e. moving with the plate over time).

3 Relationship between heat flux and lithospheric thinning

As soon the rising plume reaches the lithosphere-asthenosphere boundary, it starts to spread laterally beneath the lithosphere, either symmetrically or asymmetrically depending on whether the plate is stagnant (Figure 1a) or moving (Figure 1b-c). The temperature and viscosity anomalies related to the emplacement of hotter than ambient material beneath the lithosphere erodes the base of the lithosphere both mechanically via the formation of drips (visible as cold extensions below the lithosphere, expressed as negative values of lithospheric thinning, Figure 1), and by locally uplifting isotherms via steepening the lithospheric temperature gradient (green lines in Figure 1a-b and isosurface in Figure 1c, lower panels). Drips form predominantly next to the plume track, where the plume pushes the eroded lithosphere, but some also form in the plume-affected area downstream of the plume. The respective lithosphere thinning and surface heat flux anomalies are shown in Figure 1 above the snapshots of the temperature field. As can be seen, the patterns of heat flux and lithosphere thinning are directly comparable to each other for stagnant plate cases (Figure 1a), while the anomalies differ significantly at any given time for moving plate models (Figures 1b-c). The short wavelengths of lithosphere thinning are not reflected in the heat flux in either case.

In order to better understand the timing and relation between the thinning and heat flux anomalies, we track their evolution for two positions that move along with the plate. Figure 2 shows the relative lithosphere thinning (blue lines) and relative surface heat flux (red lines) for two 3-D cases with different plume excess temperatures. In both cases, lithosphere thinning starts significantly earlier than the onset of the surface heat flux, and may even reach a maximum value before a detectable heat flux anomaly has evolved. For most models, the maximum heat flux anomaly is delayed by about 40-140 Myr compared to the maximum lithosphere thinning, with (initially) thinner or more thinned lithosphere resulting in smaller delays. Apart from the timing, Figure 2 also shows that more extensive thinning, for example due to a hotter plume (right panel), results in a larger heat flux anomaly. The same trend can be observed by comparing different positions on the same plate, where stronger thinning is followed by a larger heat flux anomaly (dashed and solid lines in Figure 2).

4 Parameter dependence of anomalies

The amplitudes of plume-induced anomalies vary significantly among different model runs (Figures 1 and 2). Although all reference cases have exactly the same parameters (except whether the plate is moving or not), predicted anomalies are largest for stagnant plates due to the prolonged time of plume-lithosphere interaction. As a consequence, a shorter plume lifetime or a faster plate velocity reduces heat flux and thinning anomalies, while a longer plume lifetime or a lower plate velocity have the opposite effect. Apart from plate velocity, several other parameters affect how much the lithosphere is thinned by the plume, and therefore directly affect the predicted surface heat flux anomly. Figure 3 shows the temporal evolution of relative surface heat flux anomalies and relative lithosphere thinning for 6 different cases of stagnant plates. As can be seen, a lower asthenosphere viscosity facilitates lithosphere erosion (Figure 3b) and results in larger surface heat flux anomalies, as can also be seen in Figure 2. Lower lithosphere viscosity produces an even stronger trend, with a weaker lithosphere being eroded more easily (compare Figure 4 and SI Tables S2-S4). A stress-dependent (non-Newtonian) viscosity can also significantly reduce the viscosity locally above the plume due to high strain-rate (Equation (2)), resulting in stronger lithosphere thinning and elevated heat flux (Figure 4). In contrast, the plume excess temperature has a relatively minor impact on the anomalies (Figure 3c-d), especially for moving plate cases. The same holds true for the initial lithosphere or asthenosphere thickness, although the absolute thinning is smaller/bigger for thinner/thicker plates (SI Tables S2-S4). The maximum heat flux anomaly occurs many 10s of Myr after the maximum lithospheric thinning for all parameter combinations (Figure 2), consistent with our previous findings (Figure 3).

Even though the maximum anomalies of lithosphere thinning and heat flux are not observed at the same time, they are directly related. Figure 4 shows the predicted relative maximum surface heat flux anomaly as a function of maximum relative lithosphere thinning for all tested parameters and geometries. As can be seen, all models fall along the same trend, independent of the geometry (2-D or 3-D) or whether the plate is stagnant or moving, with most of the tested stagnant plate cases exhibiting significantly larger values for both anomalies compared to the corresponding moving plate cases (see also Figure 1). Models with a stagnant plate can reach heat flux anomalies of up to about 52 % (about 16.3 mW/m^2) for an asthenosphere with $\eta_{\mathrm{Asth}} = 1e18$ Pa·s (with about 39 % or 49.6 km of local thinning), or even up to 80 % (31.3 mW/m^2, with 50 % or 80 km thinning) for a model with diffusion-dislocation creep. The highest absolute heat flux of 43.7 mW/m^2 (60 % relative anomaly) is observed for a weak lower lithosphere with activation energy $E = 100$ kJ/mol, but this model features ample small-scale convection with unstable lithosphere and thus a rather unrealiable lithosphere thinning (130.4 km or 58 %). In contrast, 2-D and 3-D moving plate cases mostly cluster below heat flux anoamlies of 30 % (about 10 mW/m^2), with only very few models reaching higher values. Heat flux anomalies of 20 % or more (or at least about 6 mW/m^2) can only be reached for asthenosphere viscosities of $\eta_{\mathrm{Asth}} \leq 1e18$ Pa·s and/or a weak lower lithosphere, which might be convectively unstable anyway.

We can compare our models to an analytical solution for the time-dependent thermal structure of a stationary system. If we instantaneously offset the lithosphere-asthenosphere boundary by Δh (inlay in Figure 4) and let the system equilibrate thermally, the surface heat flux will develop a time-dependent anomaly $\Delta q(t)$. Starting from Carslaw and Jaeger (1959) Chapters 3.3 and 3.4, we can express the time-dependent temperature profile in the thinned lithosphere as

$$T(z,t) = T_0 + \frac{T_m - T_0}{l} z - \frac{2lk}{\pi} \sum_{n=1}^{\infty} \frac{(-1)^{n-1}}{n} \exp\left[\frac{-\kappa n^2 \pi^2}{l^2} t\right] \sin\left(\frac{n\pi z}{l}\right) \tag{3}$$

with the surface and LAB temperatures T_0 and T_m, the initial and reduced lithosphere thicknesses L and $l = L - \Delta h$, the thermal diffusivity κ and the differential temperature gradient $k = (T_m - T_0)\left(\frac{1}{l} - \frac{1}{L}\right)$. Using the heat flux equation $q = -K\frac{dT}{dz}$ with the thermal conductivity K at the surface ($z = 0$) and reference heat flux q_0, we obtain the relative heat flux anomaly

$$\Delta q_{rel}(t) = \frac{\Delta q}{q_0} = \frac{\Delta h_{rel}}{1 - \Delta h_{rel}} \left(1 - 2\sum_{n=1}^{\infty} (-1)^{n-1} \exp\left[-\frac{n^2\pi^2 d^2}{4}\right]\right) \tag{4}$$

as a function of relative lithosphere thinning Δh_{rel}, with the dimensionless length scale $d = \frac{2\sqrt{\kappa t}}{l} = \frac{2\sqrt{\kappa t}}{L(1-\Delta h_{rel})}$. A detailed derivation is given in the Supporting Information. In the time limits of zero ($t \rightarrow 0$, no time to equilibrate) or infinty ($t \rightarrow \infty$, fully equilibrated) time, the heat flux anomaly approaches $\Delta q_{rel} = 0$ and $\Delta q_{rel} = \frac{\Delta h_{rel}}{1-\Delta h_{rel}}$, respectively. The red line in Figure 4 represents the maximum heat flux of a fully-equilibrated system ($t \rightarrow \infty$), while the black and grey lines in Figure 4 are obtained for different values of equilibration time t assuming $L = 137.8\,\mathrm{km}$. As can be seen, the grey lines approach the maximum heat flux for larger values of t. However, none of our dynamic models reach that maximum, because the plume dynamic changes and the lithosphere starts to regrow following maximal thinning (see Figure 2). Most of our models result in anomalies similar to a stationary model equilibrating for about $40 - 100\,\mathrm{Myr}$, with an optimal value of $t = 60\,\mathrm{Myr}$.

5 Discussion

Our results show a clear causal relation between a plume eroding the lithosphere at the base, and a surface heat flux anomaly associated with the passage of a plume. In order to produce a significant heat flux anomaly ($> 30\,\%$ or $> 10\,\mathrm{mW/m^2}$), the lithosphere must be thinned by more than $30\,\%$ (about $40\,\mathrm{km}$). The trend we identify is independent of the chosen geometry or whether the plate is moving or not, and corresponds to the analytical solution for instantaneous thinning of a thermally conducting layer. However, due to the limited interaction time between plume and lithosphere, the system in our models (and in Earth) ususally cannot fully adjust thermally to the emplaced temperature anomaly before the lithosphere starts to regrow (thicken) again. As a consequence, the analytical solution can be used to estimate expected heat flux anomalies, and to place an upper bound on the pssible surface heat flux for any value of lithosphere thinning. Based on the identified trends, our results indicate that the lithosphere in dynamic models may stay sufficiently thinned for about $40 - 100\,\mathrm{Myr}$ (using Eq. (4) and $L = 137.8\,\mathrm{km}$) to evolve a correspoding heat flux anomaly before it starts to regrow again. This time frame is also approximately reflected in the delay times of heat flux anomalies ($40-140\,\mathrm{Myr}$), although these delay times are more variable because they depend on the effective lithosphere thickness and the time-integrated dynamics of the system.

Of course our analysis is simplified in several ways. One important simplification is the absence of melt, which may alter the local heat flux and its delay time significantly.

If melt intrudes into the lithosphere, hot material would infiltrate the lithosphere up to much shallower depths, rapidly increasing local heat flux without affecting lithosphere thinning (Von Herzen et al., 1989). However, for continental and especially cratonic lithosphere, intrusive volcanism may be limited (e.g. Chu et al., 2013; Yang & Leng, 2014), and extrusive volcanism is only observed in localized areas (e.g. Knott et al., 2020). As the absence of continuous volcanism indicates, the ability of melt to intrude into the lower cratonic lithosphere is reduced (Aulbach et al., 2017). As a consequence, we may expect a primarily conductive heat flux anomaly along parts of the continental plume tracks. However, future work should include melt and melt dynamics in order to understand how this can locally and regionally affect the surface heat flux.

We also did not include a variable radiogenic heat or any compositional differences within the lithosphere. A higher radiogenic heat production in the upper crust (Martos et al., 2018) would increase overall heat fluxes, and thus reduce relative heat flux anomlies, while lateral variations in radiogenic heat production can cause apparent anomalies. Otherwise, we do not expect the shallow lithospheric structure, e.g. the Moho discontinuity between the crust and the lithospheric mantle (Mordret, 2018), to have any significant effect on the predicted anomalies, except for melt intrusions. Thus, only lateral heteorgeneities in the lithospheric structure, which may include local weak zones or a pre-existing variations in lithosphere thickness, are expected to have an impact on lithospheric thinning and associated surface heat flux. In addition, anisotropic lithosphere viscosity may affect the position and dynamics of dripping instabilities (Lev & Hager, 2008; Király et al., 2020).

Finally, we can apply the identified trends to examples on Earth. Based on visual estimates of lithosphere thinning for Greenland of about 27 % (or 40 km, Celli et al. (2021)) and for South Africa of about 47 % (about 70 km, Celli et al. (2020)) for 150 km thick cratons, we would expect maximum relative heat flux anomalies of about 20 % and 60 %, respectively (Figure 4). In fact, Martos et al. (2018) infer a relative heat flux anomaly of about 25 % (assuming a maximum value of $70\,\mathrm{mW/m^2}$ and a reference value of $56\,\mathrm{mW/m^2}$). Note, however, that due to the age of the plume-lithosphere interaction (about $50-100$ Ma for Greenland (Martos et al., 2018), and $100-130$ Ma for Africa (Celli et al., 2020)), the heat flux anomaly in Greenland is likely still increasing, while the heat flux anomaly in Africa should be approximately at its maximum value or already decreasing.

6 Conclusions

The interaction between a plume and continental or cratonic lithosphere is usually less apparent than it is for oceanic lithosphere, since extrusive volcanism is less common. However, the plume still leaves a trace in form of a thinned lithosphere and a (potentially) increased surface heat flux. The emplacement of hot plume material rapidly thins the lithosphere locally, and increases the lithospheric temperature gradient over time. As a consequence, positions and amplitudes of the two anomalies are directly linked and follow the same path along the plate. However, while lithosphere thinning occurs throughout the plume-lithosphere interaction, and in most cases maximum thinning is observed within a few Myr after the plume has passed, the maximum heat flux anomaly only occurs approximately 40-140 Myr later due to the slow process of heat conduction. This has to be taken into account when interpreting geophysical data, which provide only a snapshot in time. The extent of lithosphere thinning, and thus also the amplitude of surface heat flux anomalies, is most sensitive to the viscosity of the lower lithosphere and asthenosphere, with plume excess temperature and plate velocity (for moving plate cases) or plume life time (stagnant plate cases) having secondary influence. The thicknesses of the lithosphere and asthenosphere only play a minor role.

The relation between relative surface heat flux and relative lithosphere thinning is independent of the chosen geometry, and can be approximated by an analytical expression for the time-dependent thermal structure of a stationary system. However, the lithosphere in dynamic models (and probably Earth) typically does not have time to fully equilibrate thermally, and thus does not achieve the maximum possible heat flux. In fact, most models exhibit anomalies analogous to about $40-100$ Myr of stationary thermal evolution, allowing us to predict expected and potential heat flux anomalies if the lithospheric thinning is known. This spatio-temporal relation of plume-induced lithospheric thinning and associated surface heat flux has important implications for understanding the potential of geothermal energy sources and estimating glacial melting in polar regions.

7 Open Research

All data used in this numerial modelling study can be reproduced using the information given in the text, the Supporting Information text S2 and the parameters in Table S1. An overview of the reproducible results from the numerical simulations with given parameters as shown in Figure 4 is provided in Tables S2-S4. The generated data sets are not archived in a repository since they are reproducible using the given parameters and the software ASPECT v.2.2.0, which is openly available from (Bangerth et al., 2020).

Acknowledgments

This work was supported partly by the Research Council of Norway's projects 223272 (Centre of Excellence) and 288449 (MAGPIE Project), and by the European Space Agency (ESA). This work was carried out as part of the European Space Agency's Support to Science Element "3D Earth – A dynamic living planet". Computations were made possible by the Norwegian Research Infrastructure Services (NRIS) via allocations NN9283K/ NS9029K. We thank the Computational Infrastructure for Geodynamics (geodynamics.org), which is funded by the National Science Foundation under award EAR-0949446 and EAR-1550901, for supporting the development of ASPECT.

References

Albers, M., & Christensen, U. R. (1996). The excess temperature of plumes rising from the core-mantle boundary. *Geophysical Research Letters*, *23*(24), 3567–3570. Retrieved from `https://agupubs.onlinelibrary.wiley.com/doi/abs/10.1029/96GL03311` doi: 10.1029/96GL03311

Aulbach, S., Massuyeau, M., & Gaillard, F. (2017). Origins of cratonic mantle discontinuities: A view from petrology, geochemistry and thermodynamic models. *Lithos*, *268-271*, 364–382. Retrieved from `http://www.sciencedirect.com/science/article/pii/S0024493716303905` doi: 10.1016/j.lithos.2016.11.004

Ballmer, M. D., Ito, G., van Hunen, J., & Tackley, P. J. (2011). Spatial and temporal variability in hawaiian hotspot volcanism induced by small-scale convection. *Nature Geoscience*, *4*(7), 457–460. doi: 10.1038/ngeo1187

Bangerth, W., Dannberg, J., Gassmoeller, R., & Heister, T. (2020, June). *Aspect v2.2.0.* Zenodo. Retrieved from `https://doi.org/10.5281/zenodo.3924604` doi: 10.5281/zenodo.3924604

Bono, R. K., Tarduno, J. A., & Bunge, H.-P. (2019). Hotspot motion caused the hawaiian-emperor bend and llsvps are not fixed. *Nature Communications*, *10*(1), 3370. doi: 10.1038/s41467-019-11314-6;10.1038/s41467-019-11314-6

Carslaw, H. S., & Jaeger, J. C. (1959). *Conduction of heat in solids.* Oxford University Press.

Celli, N. L., Lebedev, S., Schaeffer, A. J., & Gaina, C. (2020). African cratonic lithosphere carved by mantle plumes. *Nature Communications*, *11*(1), 92. doi: 10.1038/s41467-019-13871-2

Celli, N. L., Lebedev, S., Schaeffer, A. J., & Gaina, C. (2021). The tilted iceland plume and its effect on the north atlantic evolution and magmatism. *Earth and Planetary Science Letters*, *569*, 117048. Retrieved from `https://www.sciencedirect.com/science/article/pii/S0012821X21003034` doi: 10.1016/j.epsl.2021.117048

Chang, S.-J., Kendall, E., Davaille, A., & Ferreira, A. M. G. (2020). The evolution of mantle plumes in east africa. *Journal of Geophysical Research: Solid Earth*, *125*(12), e2020JB019929. Retrieved from `https://agupubs.onlinelibrary.wiley.com/doi/abs/10.1029/2020JB019929` (e2020JB019929 2020JB019929) doi: 10.1029/2020JB019929

Chu, R., Leng, W., Helmberger, D. V., & Gurnis, M. (2013). Hidden hotspot track beneath the eastern united states. *Nature Geoscience*, *6*(11), 963–966. doi: 10.1038/ngeo1949

Colgan, W., Wansing, A., Mankoff, K., Lösing, M., Hopper, J., Louden, K., . . . Løkkegaard, A. (2021). Greenland geothermal heat flow database and map (version 1). *Earth System Science Data Discussions*, *2021*, 1–50. Retrieved from `https://essd.copernicus.org/preprints/essd-2021-290/` doi: 10.5194/essd-2021-290

Dannberg, J., & Gassmöller, R. (2018). Chemical trends in ocean islands explained by plume–slab interaction. *Proceedings of the National Academy of Sciences*, *115*(17), 4351–4356. Retrieved from `https://www.pnas.org/content/115/17/4351` doi: 10.1073/pnas.1714125115

Davies, G. F. (1994). Thermomechanical erosion of the lithosphere by mantle plumes. *Journal of Geophysical Research: Solid Earth*, *99*(B8), 15709–15722. Retrieved from `https://agupubs.onlinelibrary.wiley.com/doi/abs/10.1029/94JB00119` doi: 10.1029/94JB00119

Doubrovine, P. V., Steinberger, B., & Torsvik, T. H. (2012). Absolute plate motions in a reference frame defined by moving hot spots in the pacific, atlantic, and indian oceans. *Journal of Geophysical Research: Solid Earth*, *117*(B9). Retrieved from https://agupubs.onlinelibrary.wiley.com/doi/abs/10.1029/2011JB009072 doi: 10.1029/2011JB009072

Hansen, S. E., Nyblade, A. A., & Benoit, M. H. (2012). Mantle structure beneath africa and arabia from adaptively parameterized p-wave tomography: Implications for the origin of cenozoic afro-arabian tectonism. *Earth and Planetary Science Letters*, *319-320*, 23–34. Retrieved from http://www.sciencedirect.com/science/article/pii/S0012821X11007436 doi: 10.1016/j.epsl.2011.12.023

Harrison, L. N., Weis, D., & Garcia, M. O. (2017). The link between hawaiian mantle plume composition, magmatic flux, and deep mantle geodynamics. *Earth and Planetary Science Letters*, *463*, 298–309. Retrieved from http://www.sciencedirect.com/science/article/pii/S0012821X17300390 doi: 10.1016/j.epsl.2017.01.027

Heister, T., Dannberg, J., Gassmöller, R., & Bangerth, W. (2017). High accuracy mantle convection simulation through modern numerical methods. II: Realistic models and problems. *Geophysical Journal International*, *210*(2), 833–851. Retrieved from https://doi.org/10.1093/gji/ggx195 doi: 10.1093/gji/ggx195

Huang, S., Hall, P. S., & Jackson, M. G. (2011, September). Geochemical zoning of volcanic chains associated with pacific hotspots. *Nature Geoscience*, *4*, 874–878. Retrieved from https://www.nature.com/articles/ngeo1263\#supplementary-information doi: 10.1038/ngeo1263;10.1038/ngeo1263

Hui, H., Peslier, A. H., Rudnick, R. L., Simonetti, A., & Neal, C. R. (2015). Plume-cratonic lithosphere interaction recorded by water and other trace elements in peridotite xenoliths from the labait volcano, tanzania. *Geochemistry, Geophysics, Geosystems*, *16*(6), 1687–1710. Retrieved from https://agupubs.onlinelibrary.wiley.com/doi/abs/10.1002/2015GC005779 doi: 10.1002/2015GC005779

Jean, M. M., Hanan, B. B., & Shervais, J. W. (2014). Yellowstone hotspot–continental lithosphere interaction. *Earth and Planetary Science Letters*, *389*, 119–131. Retrieved from http://www.sciencedirect.com/science/article/pii/S0012821X13007188 doi: 10.1016/j.epsl.2013.12.012

King, S. D., & Adam, C. (2014). Hotspot swells revisited. *Physics of the Earth and Planetary Interiors*, *235*, 66–83. Retrieved from http://www.sciencedirect.com/science/article/pii/S0031920114001642 doi: 10.1016/j.pepi.2014.07.006

Király, Á., Conrad, C. P., & Hansen, L. N. (2020). Evolving viscous anisotropy in the upper mantle and its geodynamic implications. *Geochemistry, Geophysics, Geosystems*, *21*(10), e2020GC009159. Retrieved from https://agupubs.onlinelibrary.wiley.com/doi/abs/10.1029/2020GC009159 (e2020GC009159 2020GC009159) doi: 10.1029/2020GC009159

Knott, T. R., Branney, M. J., Reichow, M. K., Finn, D. R., Tapster, S., & Coe, R. S. (2020, June). Discovery of two new super-eruptions from the yellowstone hotspot track (usa): Is the yellowstone hotspot waning? *Geology*, *48*(9), 934–938. doi: 10.1130/G47384.1

Koptev, A., Burov, E., Calais, E., Leroy, S., Gerya, T., Guillou-Frottier, L., & Cloetingh, S. (2016). Contrasted continental rifting via plume-craton interaction: Applications to central east african rift. *Geoscience Frontiers*, *7*(2), 221–236. Retrieved from http://www.sciencedirect.com/science/article/pii/S1674987115001280 (Special Issue: Exhuming Asia) doi: 10.1016/j.gsf.2015.11.002

Kronbichler, M., Heister, T., & Bangerth, W. (2012). High accuracy mantle convection simulation through modern numerical methods. *Geophysical Journal International*, *191*, 12–29. Retrieved from http://dx.doi.org/10.1111/j.1365-246X.2012.05609.x doi: 10.1111/j.1365-246X.2012.05609.x

Lev, E., & Hager, B. H. (2008). Rayleigh–taylor instabilities with anisotropic lithospheric viscosity. *Geophysical Journal International*, *173*(3), 806–814. Retrieved from https://onlinelibrary.wiley.com/doi/abs/10.1111/j.1365-246X.2008.03731.x doi: 10.1111/j.1365-246X.2008.03731.x

Liu, J., Pearson, D. G., Wang, L. H., Mather, K. A., Kjarsgaard, B. A., Schaeffer, A. J., . . . Armstrong, J. P. (2021). Plume-driven recratonization of deep continental lithospheric mantle. *Nature*, *592*(7856), 732–736. doi: 10.1038/s41586-021-03395-5

Lösing, M., Ebbing, J., & Szwillus, W. (2020). Geothermal heat flux in antarctica: Assessing models and observations by bayesian inversion. *Frontiers in Earth*

Science, *8*, 105. Retrieved from https://www.frontiersin.org/article/10.3389/feart.2020.00105 doi: 10.3389/feart.2020.00105

Martos, Y. M., Jordan, T. A., Catalán, M., Jordan, T. M., Bamber, J. L., & Vaughan, D. G. (2018). Geothermal heat flux reveals the iceland hotspot track underneath greenland. *Geophysical Research Letters*, *45*(16), 8214–8222. Retrieved from https://agupubs.onlinelibrary.wiley.com/doi/abs/10.1029/2018GL078289 doi: 10.1029/2018GL078289

Mordret, A. (2018). Uncovering the iceland hot spot track beneath greenland. *Journal of Geophysical Research: Solid Earth*, *123*(6), 4922–4941. Retrieved from https://agupubs.onlinelibrary.wiley.com/doi/abs/10.1029/2017JB015104 doi: 10.1029/2017JB015104

Morgan, W. J. (1971). Convection plumes in the lower mantle. *Nature*, *230*(5288), 42–43. doi: 10.1038/230042a0

Paul, J., & Ghosh, A. (2021, 12). Could the réunion plume have thinned the indian craton? *Geology*. Retrieved from https://doi.org/10.1130/G49492.1 doi: 10.1130/G49492.1

Polat, A., Li, J., Fryer, B., Kusky, T., Gagnon, J., & Zhang, S. (2006). Geochemical characteristics of the neoarchean (2800–2700 ma) taishan greenstone belt, north china craton: Evidence for plume–craton interaction. *Chemical Geology*, *230*(1), 60–87. Retrieved from http://www.sciencedirect.com/science/article/pii/S0009254105005206 doi: 10.1016/j.chemgeo.2005.11.012

Richards, M. A., Duncan, R. A., & Courtillot, V. E. (1989). Flood basalts and hotspot tracks: Plume heads and tails. *Science*, *246*(4926), 103–107. Retrieved from http://www.jstor.org/stable/1703920

Rogozhina, I., Petrunin, A. G., Vaughan, A. P. M., Steinberger, B., Johnson, J. V., Kaban, M. K., … Koulakov, I. (2016). Melting at the base of the greenland ice sheet explained by iceland hotspot history. *Nature Geoscience*, *9*(5), 366–369. doi: 10.1038/ngeo2689;10.1038/ngeo2689

Rysgaard, S., Bendtsen, J., Mortensen, J., & Sejr, M. K. (2018). High geothermal heat flux in close proximity to the northeast greenland ice stream. *Scientific Reports*, *8*(1), 1344. doi: 10.1038/s41598-018-19244-x;10.1038/s41598-018-19244-x

Seroussi, H., Ivins, E. R., Wiens, D. A., & Bondzio, J. (2017). Influence of a west antarctic mantle plume on ice sheet basal conditions. *Journal of Geophysical Research: Solid Earth*, *122*(9), 7127–7155. Retrieved from https://agupubs.onlinelibrary.wiley.com/doi/abs/10.1002/2017JB014423 doi: 10.1002/2017JB014423

Sharma, J., Kumar, M. R., Roy, K. S., & Roy, P. N. S. (2018). Seismic imprints of plume-lithosphere interaction beneath the northwestern deccan volcanic province. *Journal of Geophysical Research: Solid Earth*, *123*(12), 10,831–10,853. Retrieved from https://agupubs.onlinelibrary.wiley.com/doi/abs/10.1029/2018JB015947 doi: 10.1029/2018JB015947

Shen, W., Wiens, D. A., Lloyd, A. J., & Nyblade, A. A. (2020). A geothermal heat flux map of antarctica empirically constrained by seismic structure. *Geophysical Research Letters*, *47*(14), e2020GL086955. Retrieved from https://agupubs.onlinelibrary.wiley.com/doi/abs/10.1029/2020GL086955 (e2020GL086955 2020GL086955) doi: 10.1029/2020GL086955

Shervais, J. W., & Hanan, B. B. (2008). Lithospheric topography, tilted plumes, and the track of the snake river–yellowstone hot spot. *Tectonics*, *27*(5). Retrieved from https://agupubs.onlinelibrary.wiley.com/doi/abs/10.1029/2007TC002181 doi: 10.1029/2007TC002181

Smith-Johnsen, S., Schlegel, N.-J., de Fleurian, B., & Nisancioglu, K. H. (2020). Sensitivity of the northeast greenland ice stream to geothermal heat. *Journal of Geophysical Research: Earth Surface*, *125*(1), e2019JF005252. Retrieved from https://agupubs.onlinelibrary.wiley.com/doi/abs/10.1029/2019JF005252 (e2019JF005252 10.1029/2019JF005252) doi: 10.1029/2019JF005252

Torsvik, T. H., Steinberger, B., Ashwal, L. D., Doubrovine, P. V., & Trønnes, R. G. (2016). Earth evolution and dynamics—a tribute to kevin burke. *Canadian Journal of Earth Sciences*, *53*(11), 1073–1087. Retrieved from https://doi.org/10.1139/cjes-2015-0228 doi: 10.1139/cjes-2015-0228

Von Herzen, R. P., Cordery, M. J., Detrick, R. S., & Fang, C. (1989). Heat flow and the thermal origin of hot spot swells: The hawaiian swell revisited. *Journal of Geophysical Research: Solid Earth*, *94*(B10), 13783–13799. Retrieved from https://agupubs.onlinelibrary.wiley.com/doi/abs/10.1029/JB094iB10p13783 doi: 10.1029/JB094iB10p13783

Wang, W., Liu, S., Santosh, M., Wang, G., Bai, X., & Guo, R. (2015). Neoarchean intra-oceanic arc system in the western liaoning province: Implications for early precambrian crustal evolution in the eastern block of the north china craton. *Earth-Science Reviews*, *150*, 329–364. Retrieved from http://www.sciencedirect.com/science/article/pii/S001282521530026X doi: 10.1016/j.earscirev.2015.08.002

Yang, T., & Leng, W. (2014). Dynamics of hidden hotspot tracks beneath the continental lithosphere. *Earth and Planetary Science Letters*, *401*, 294–300. Retrieved from https://www.sciencedirect.com/science/article/pii/S0012821X14003963 doi: 10.1016/j.epsl.2014.06.019

Yuan, H., Dueker, K., & Stachnik, J. (2010). Crustal structure and thickness along the yellowstone hot spot track: Evidence for lower crustal outflow from beneath the eastern snake river plain. *Geochemistry, Geophysics, Geosystems*, *11*(3). Retrieved from https://agupubs.onlinelibrary.wiley.com/doi/abs/10.1029/2009GC002787 doi: 10.1029/2009GC002787

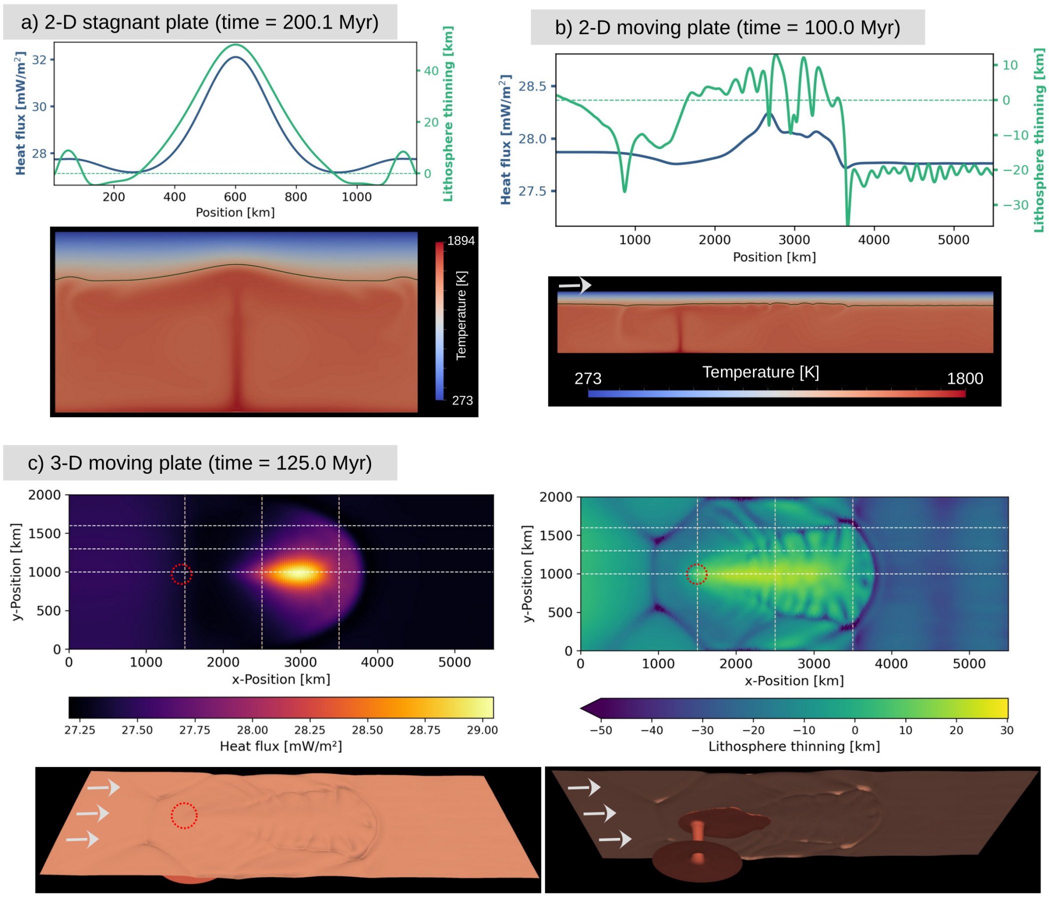

Figure 1. Snapshots of the temperature field of our (a) 2-D stagnant, (b) 2-D moving and (c) 3-D moving plate reference cases, together with the respective lithosphere thinning and heat flux at given times after plume initiation. Negative thinning indicates local thickening of the plate, for example by the formation of drips. The bottom panels in (c) show the isotherms of 1400 K and 1600 K at the same time step, once from above (left) and once from below (right), and the green lines in (a) and (b) mark the 1400 K isotherm. The red circles in (c) mark the position of the plume, and grey arrows indicate plate velocity.

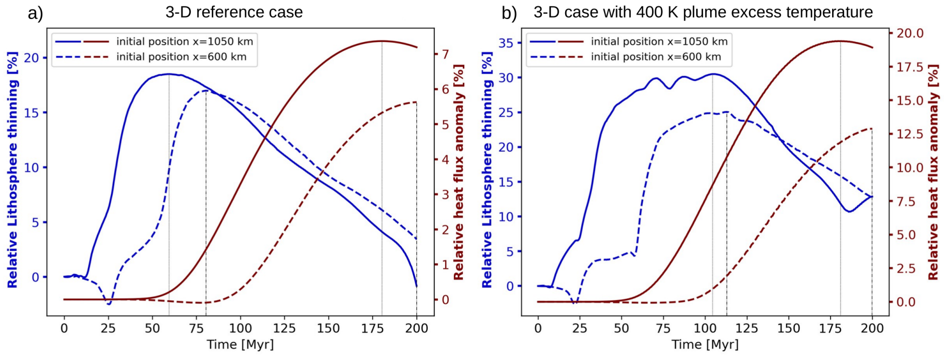

551 **Figure 2.** Relative surface heat flux (red) and relative lithosphere thinning (blue) versus time after plume initiation for two posititons along the central profile (y=1000 km) fixed to the 3-D moving plate. The starting positions at t=0 are x=600 km and x=1050 km, and thus 900 km and 450 km upstream (left) of the plume, respectively. (a) is taken for the 3-D reference case (Figure 1c, with plume excess temperature of 250 K), while (b) represents a model with a plume excess temperature of 400 K. Vertical dashed lines mark the times of maxima.

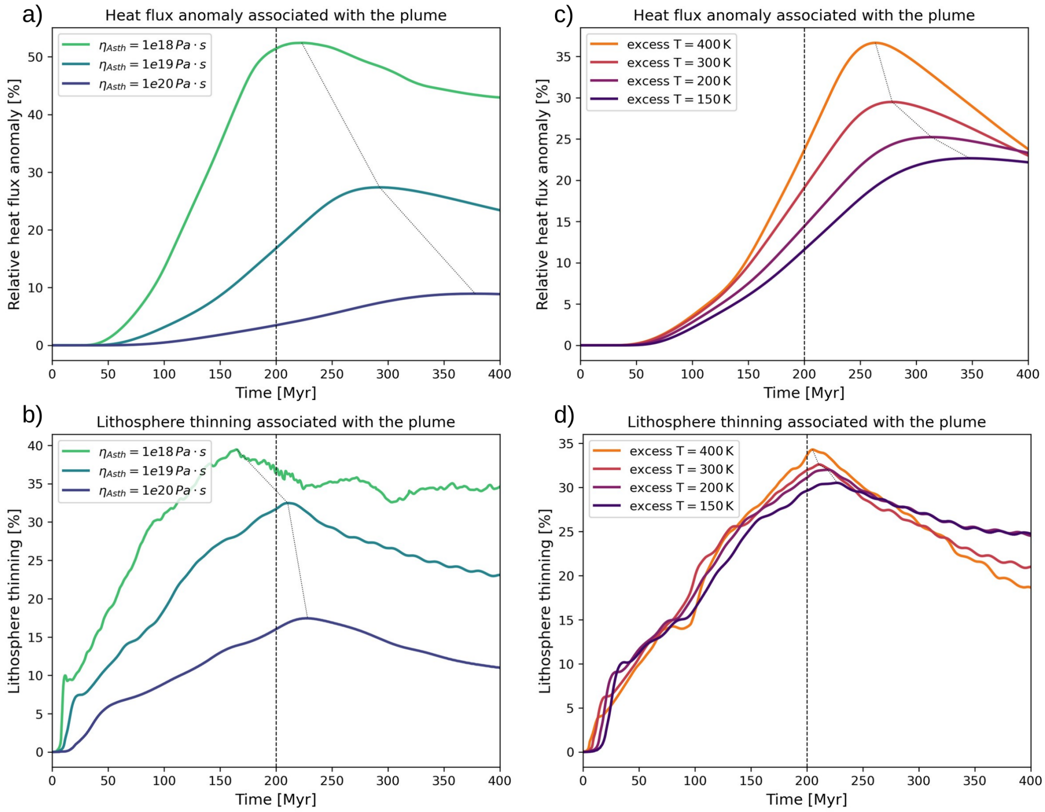

557 **Figure 3.** Maximum relative surface heat flux anomalies (top) and maximum relative lithosphere thinning (bottom) versus time for different 2-D stagnant plate models, measured above the plume center. The grey dashed line marks the respective positions of maxima. (a) and (b) show the temporal evolution of models with three different asthenosphere viscosities, with $\eta_{\mathrm{Asth}} = 1e19\,\mathrm{Pa{\cdot}s}$ representing the reference case shown in Figure 1a. (c) and (d) are obtained for models with different plume excess temperatures. The reference case has a plume excess temperature of 250 K and is not shown in this panel.

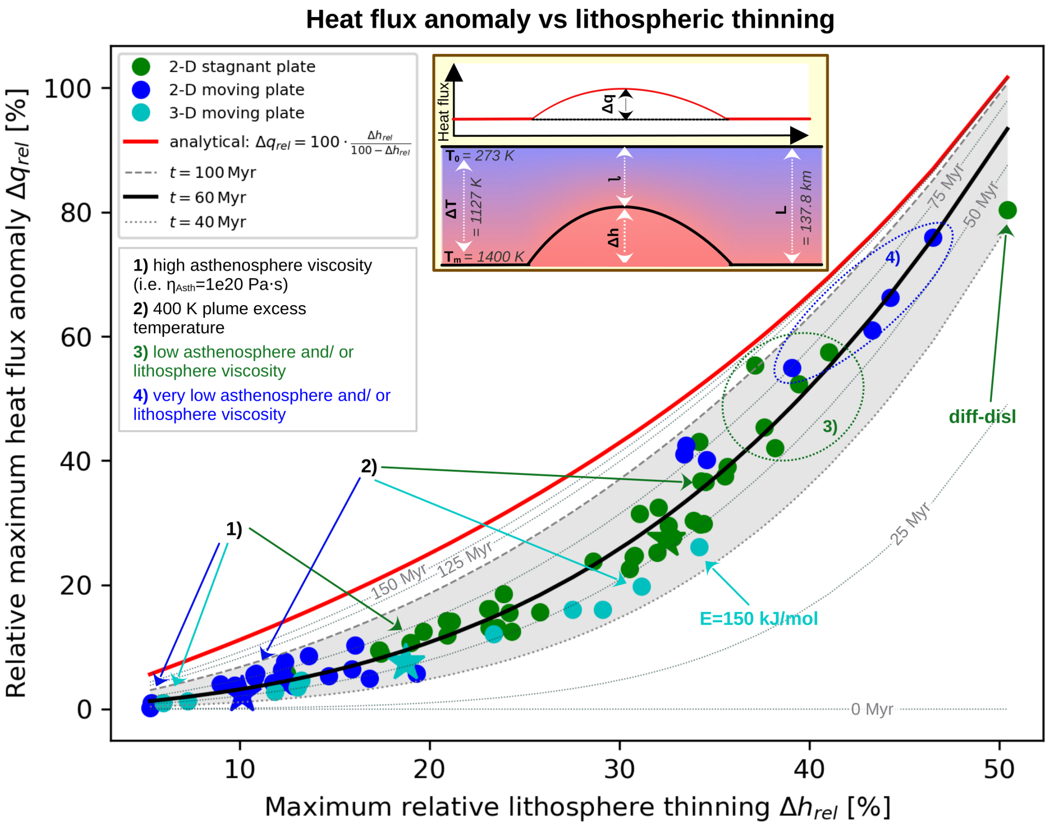

Figure 4. Summary of the relation between maximum relative lithospheric thinning and maximum relative heat flux anomaly for all tested models in 2-D and 3-D geometries. For comparison, the analytical solution (Equation (4)) for an initial lithosphere thickness $L = 137.8\,\mathrm{km}$ and $\kappa = 0.8 \cdot 10^{-6}\,\mathrm{m^2/s}$ is plotted for $t \to \infty$ (red line), $t = 60\,\mathrm{Myr}$ (black line), and 25 Myr steps between 0 and 150 Myr (grey lines). The shaded area between $t = 40\,\mathrm{Myr}$ (dotted line) and $t = 100\,\mathrm{Myr}$ (dashed line) encloses most of the tested models. Groups of points with specific shared characteristics are marked and explained in legend. The inlay cartoon defines the parameters in the analytical solution for the instantaneous lithospheric thinning.

Supporting Information for "On the relation between lithosphere thickness and surface heat flux for continental plume tracks"

Björn H. Heyn [1], Clinton P. Conrad [1]

[1]Centre for Earth Evolution and Dynamics (CEED), University of Oslo, Norway

Contents of this file

1. Text S1 to S2
2. Figures S1 to S3
3. Tables S1 to S4

Introduction This Supporting Information provides additional information required to reproduce the results shown in the paper. Text S1 describes the derivation of the analytical solution expressed in Eqs. (3) and (4) in the main text, and used in Figure 4. We include additional Figures S1-S3 to show how the relative heat flux anomaly behaves with non-dimensional length scale d (Figure S1), and the relative thinning Δh_{rel} (Figure S2), and show how the equilibration time changes with d and Δh_{rel} (Figure S3). Furthermore, Text S2 and Table S1 provides a more detailed description of the models and the necessary parameters to run the simulations, and Table S2-S4 give the data points used in Figure 4.

Text S1. In order to derive an analytical solution for the temperature profile and the heat flux that follow instantaneous lithospheric thinning, we assume a stationary model, i.e. a model without convection. As a consequence, the temperature and heat flux change solely due to thermal conduction. For the initial undisturbed lithosphere, the equilibrated temperature profile in the lithosphere is given as

$$T(z,t) = T_0 + \frac{T_m - T_0}{L} z, \tag{1}$$

with the surface and LAB temperatures T_0 and T_m and the lithosphere thickness L. If we then thin lithosphere to a new thickness $l = L - \Delta h$ (see inlay in Figure 4) and let the system equilibrate for an infinite amount of time, the equilibrated temperature profile would be

$$T(z,t) = T_0 + \frac{T_m - T_0}{l} z. \tag{2}$$

Following the approach of Carslaw and Jaeger (1959) Chapter 3.4 for a case with initial temperature profile $f(x)$ and with ends kept at a fixed temperatures T_0 and T_m, we can split the solution into two parts $T(z,t) = u(z,t) + w(z,t)$, with $u(z,t)$ and $w(z,t)$ chosen such that

$$\frac{d^2u}{dx^2} = 0$$
$$u(0,t) = T_0$$
$$u(l,t) = T_m$$
$$\frac{\partial w}{\partial t} = \kappa \frac{d^2w}{dx^2}$$
$$w(0,t) = w(l,t) = 0$$
$$w(z,0) = f(x) - u(z,0)$$

In our case, this translates to the boundary and initial conditions

$$T(0,t) = T_0 \tag{3}$$
$$T(l,t) = T_m \tag{4}$$
$$T(z,0) = T_0 + \frac{T_m - T_0}{L} z \qquad \text{(same as Equation (1))} \tag{5}$$

and the additional constraint that

$$T(z,\infty) = T_0 + \frac{T_m - T_0}{l} z \qquad \text{(same as Equation (2)).} \tag{6}$$

Using the solution for the linear temperature profile in Carslaw and Jaeger (1959) Chapter 3.3

$$f(z) = kz = \sum_{n=1}^{\infty} a_n \sin\left(\frac{n\pi z}{l}\right) = \frac{2lk}{\pi} \sum_{n=1}^{\infty} \frac{(-1)^{n-1}}{n} \sin\left(\frac{n\pi z}{l}\right), \tag{7}$$

we find

$$u(z,t) = T_0 + \frac{T_m - T_0}{l} z$$
$$w(z,t) = -\frac{2lk^{\infty}}{\sum_{n=1}} \frac{(-1)^{n-1}}{n} \exp\left[\frac{-\kappa n^2\pi^2}{l^2} t\right] \sin\left(\frac{n\pi z}{l}\right)$$

with thermal diffusivity κ. Finally, we can then express the temperature profile as a function of time and depth via

$$T(z,t) = T_0 + \frac{T_m - T_0}{l} z - \frac{2lk}{\pi} \sum_{n=1}^{\infty} \frac{(-1)^{n-1}}{n} \exp\left[-\frac{\kappa n^2 \pi^2}{l^2} t\right] \sin\left(\frac{n\pi z}{l}\right). \qquad (8)$$

Our temperature gradient k is the differential gradient between Equations (1) and (2) and can be calculated via

$$\begin{aligned} k &= \frac{\Delta T}{l} = \frac{T_m - T^*}{l} = \frac{1}{l}\left(T_m - T_0 - \frac{T_m - T_0}{L} l\right) = \frac{1}{l}(T_m - T_0)(1 - \frac{l}{L}) \\ &= (T_m - T_0)\left(\frac{1}{l} - \frac{1}{L}\right), \end{aligned}$$

with $T^* = T(l,0) = T_0 - \frac{T_m - T_0}{L} l$ from Equation (1).

With respect to our boundary and initial conditions (Equations (3)-(6)), we get

$$\begin{aligned} Eq.(3): T(0,t) &= T_0 + \underbrace{\left(\frac{T_m - T_0}{l} 0\right)}_{=0} - \underbrace{\left(\frac{2lk}{\pi} \sum_{n=1}^{\infty} \frac{(-1)^{n-1}}{n} \exp\left[-\frac{\kappa n^2 \pi^2}{l^2} t\right] \sin\left(\frac{n\pi 0}{l}\right)\right)}_{=0} \\ &= T_0 \\ Eq.(4): T(l,t) &= T_0 + \underbrace{\left(\frac{T_m - T_0}{l} l\right)}_{=T_m - T_0} - \underbrace{\left(\frac{2lk}{\pi} \sum_{n=1}^{\infty} \frac{(-1)^{n-1}}{n} \exp\left[-\frac{\kappa n^2 \pi^2}{l^2} t\right] \sin\left(\frac{n\pi l}{l}\right)\right)}_{=0} \\ &= T_m \\ Eq.(5): T(z,0) &= T_0 + \left(\frac{T_m - T_0}{l} z\right) - \underbrace{\left(\frac{2lk}{\pi} \sum_{n=1}^{\infty} \frac{(-1)^{n-1}}{n} \exp\left[-\frac{\kappa n^2 \pi^2}{l^2} 0\right] \sin\left(\frac{n\pi z}{l}\right)\right)}_{\text{Eq. (7): } = kz = (T_m - T_0)\left(\frac{1}{l} - \frac{1}{L}\right) z} \\ &= T_0 + \frac{T_m - T_0}{L} z \\ Eq.(6): \lim_{t\to\infty} T(z,t) &= T_0 + \left(\frac{T_m - T_0}{l} z\right) - \underbrace{\lim_{t\to\infty} \left(\frac{2lk}{\pi} \sum_{n=1}^{\infty} \frac{(-1)^{n-1}}{n} \exp\left[-\frac{\kappa n^2 \pi^2}{l^2} t\right] \sin\left(\frac{n\pi z}{l}\right)\right)}_{=0} \\ &= T_0 + \frac{T_m - T_0}{l} z \end{aligned}$$

In order to obtain the heat flux, we use the heat flux equation $q = -K\frac{dT}{dz}$ with thermal conductivity K

$$q(z,t) = \frac{T_m - T_0}{l} - 2k\sum_{n=1}^{\infty}(-1)^{n-1}\exp\left[-\frac{\kappa n^2\pi^2}{l^2}t\right]\cos\left(\frac{n\pi z}{l}\right)$$

At the surface ($z = 0$), this simplifies to

$$q(0,t) = \frac{T_m - T_0}{l} - 2k\sum_{n=1}^{\infty}(-1)^{n-1}\exp\left[-\frac{\kappa n^2\pi^2}{l^2}t\right]. \tag{9}$$

We then introduce the non-dimensional length scale

$$d = 2\frac{\sqrt{\kappa t}}{l} \tag{10}$$

and express k in terms of relative thinning

$$\begin{aligned} k &= (T_m - T_0)\left(\frac{1}{l} - \frac{1}{L}\right) = (T_m - T_0)\left(\frac{L-l}{Ll}\right) \\ &\underbrace{=}_{L-l=\Delta h} \frac{T_m - T_0}{l}\Delta h_{rel}. \end{aligned}$$

Using this, we can calculate the plume-induced heat flux anomaly $\Delta q = q - q_0$ relative to the undisturbed heat flux q_0 as

$$\begin{aligned} \Delta q_{rel}(0,t) &= \frac{\Delta q}{q_0} = \frac{q}{q_0} - 1 \\ &= \frac{\frac{T_m - T_0}{l} - 2\frac{T_m - T_0}{l}\Delta h_{rel}\sum_{n=1}^{\infty}(-1)^{n-1}\exp\left[-\frac{n^2\pi^2}{4}d^2\right]}{\frac{T_m - T_0}{L}} - 1 \\ &= \frac{L}{l} - 2\frac{L}{l}\Delta h_{rel}\sum_{n=1}^{\infty}(-1)^{n-1}\exp\left[-\frac{n^2\pi^2}{4}d^2\right] - 1 \\ &= \Delta h_{rel}\frac{L}{l} - 2\frac{L}{l}\Delta h_{rel}\sum_{n=1}^{\infty}(-1)^{n-1}\exp\left[-\frac{n^2\pi^2}{4}d^2\right] \\ &= \Delta h_{rel}\frac{L}{l}\left(1 - 2\sum_{n=1}^{\infty}(-1)^{n-1}\exp\left[-\frac{n^2\pi^2}{4}d^2\right]\right) \\ \Delta q_{rel}(0,t) &= \frac{\Delta h_{rel}}{1 - \Delta h_{rel}}\left(1 - 2\sum_{n=1}^{\infty}(-1)^{n-1}\exp\left[-\frac{n^2\pi^2}{4}d^2\right]\right). \end{aligned} \tag{11}$$

Here, we used the relations

$$\frac{L}{l} - 1 = \frac{L-l}{l} \cdot \frac{L}{L} = \frac{L-l}{L} \cdot \frac{L}{l} = \Delta h_{rel} \frac{L}{l} \qquad \text{and}$$
$$\Delta h_{rel} \frac{L}{l} = \frac{\Delta h_{rel}}{\frac{l}{L}} = \frac{\Delta h_{rel}}{\frac{L}{L} - \frac{L-l}{l}} = \frac{\Delta h_{rel}}{1 - \Delta h_{rel}}.$$

In the limits of $t = 0$ and $t \to \infty$ (and thus $d = 0$ and $d \to \infty$), we obtain the heat flux anomalies

$$\begin{aligned} \Delta q_{rel}(0,0) &= \frac{\Delta h_{rel}}{1 - \Delta h_{rel}} \left(1 - 2 \underbrace{\sum_{n=1}^{\infty} (-1)^{n-1} \exp\left[-\frac{n^2 \pi^2}{4} 0^2 \right]}_{=1/2} \right) \\ &= 0 \end{aligned} \tag{12}$$

$$\begin{aligned} \Delta q_{rel}(0, t \to \infty) &= \frac{\Delta h_{rel}}{1 - \Delta h_{rel}} \left(1 - 2 \underbrace{\lim_{d \to \infty} \sum_{n=1}^{\infty} (-1)^{n-1} \exp\left[-\frac{n^2 \pi^2}{4} d^2 \right]}_{=0} \right) \\ &= \frac{\Delta h_{rel}}{1 - \Delta h_{rel}} \end{aligned} \tag{13}$$

Figure S1 shows the evolution of the relative heat flux anomaly (Eq. (11)) versus d (and thus versus time, compare Eq. (10)) for different values of relative lithosphere thinning. As can be seen, all curves asymptotically approach their maximum value before $d = 2$, although models with more thinning require more time to reach that maximum. The same behaviour for d can be seen when plotting relative heat flux amomaly Δq_{rel} versus relative thinning Δh_{rel}, see Figure S2. Again, a value of $d = 2$ predicts basically the same anomalies as a value of $d \to \infty$ (shown as dashed line in Figure S2).

Finally, we can convert the value of d to a theoretical equilibration time of a stationary model via Equation (10):

$$t = d^2 \frac{l^2}{4\kappa} = d^2 \frac{(L-\Delta h)^2}{4\kappa} \cdot \frac{L^2}{L^2}$$
$$= d^2 \frac{L^2(1-\Delta h_{rel})^2}{4\kappa}$$

As can be seen in S3, the required equilibration time decreases with increasing lithosphere thinning or decreasing value of d.

For Figure 4 in the main text, we assumed a constant equilibration time, a constant value of $L = 137.8\,\mathrm{km}$ and then used Equation (10) to calculate the corresponding value of d depending on the relative thinning Δh_{rel}:

$$d = 2\frac{\sqrt{\kappa t}}{l} = 2\sqrt{\kappa t}\frac{1}{L-(L-l)} = 2\sqrt{\kappa t}\frac{1}{L-(L-l)} \cdot \frac{1}{\frac{L}{L}} = 2\sqrt{\kappa t}\frac{1}{L - L\frac{L-l}{L}}$$
$$= 2\sqrt{\kappa t}\frac{1}{L(1-\Delta h_{rel})}$$

This can be used as input to Equation (11) to obtain the lines for constant t shown in Figure 4.

Text S2. Our 2-D stagnant plate models have domain sizes of 1200x600 km (x by z), 2-D moving plate cases are 5500x800 km (x by z) and 3-D moving plate cases are 5500x2000x800 km (x by y by z). For models with 3 cm/yr plate velocity, we had to increase the domain size to 5500x1100 km to avoid that the temperature anoamly is sheared at the bottom. The viscosity is implemented via equations (1) and (2) in the main text, with a step-wise implementation of depth-depdencen via η_j. η_j is the scaling viscosity for the two layers we have: layer one ($j = 1$) reaching from the surface down to the bottom of the asthenosphere, and layer two ($j = 2$) for the domain below the asthenosphere.

The surface temperature is fixed to 273 K for all models, while the LAB temperature (in the reference models at 150 km depth) is set to either 1500 K or 1623 K. Below the LAB, the initial temperature profile has a small temperature gradient to facilitate plume rise. Although the details of this gradient vary sligthly between stagnant (respective bottom temperatures of 1623 K or 1650 K) and moving plate cases (bottom temperatures of 1550 K and 1650 K) due to numerical stability of the solution, this does not affect the results of plume-lithosphere interaction. At the bottom, we further add a temperature anomaly of Gaussian shape ($T_p \cdot \exp\left[-\frac{(x-s)^2}{2*w^2}\right]$) with plume excess temperature T_p, width $w = 500$ km for stagnant plates ($w = 300$ km for moving plate cases) and shift $s = 600$ km ($s = 1500$ km for moving plates) to trigger and sustain a plume.

References

Carslaw, H. S., & Jaeger, J. C. (1959). *Conduction of heat in solids.* Oxford University Press.

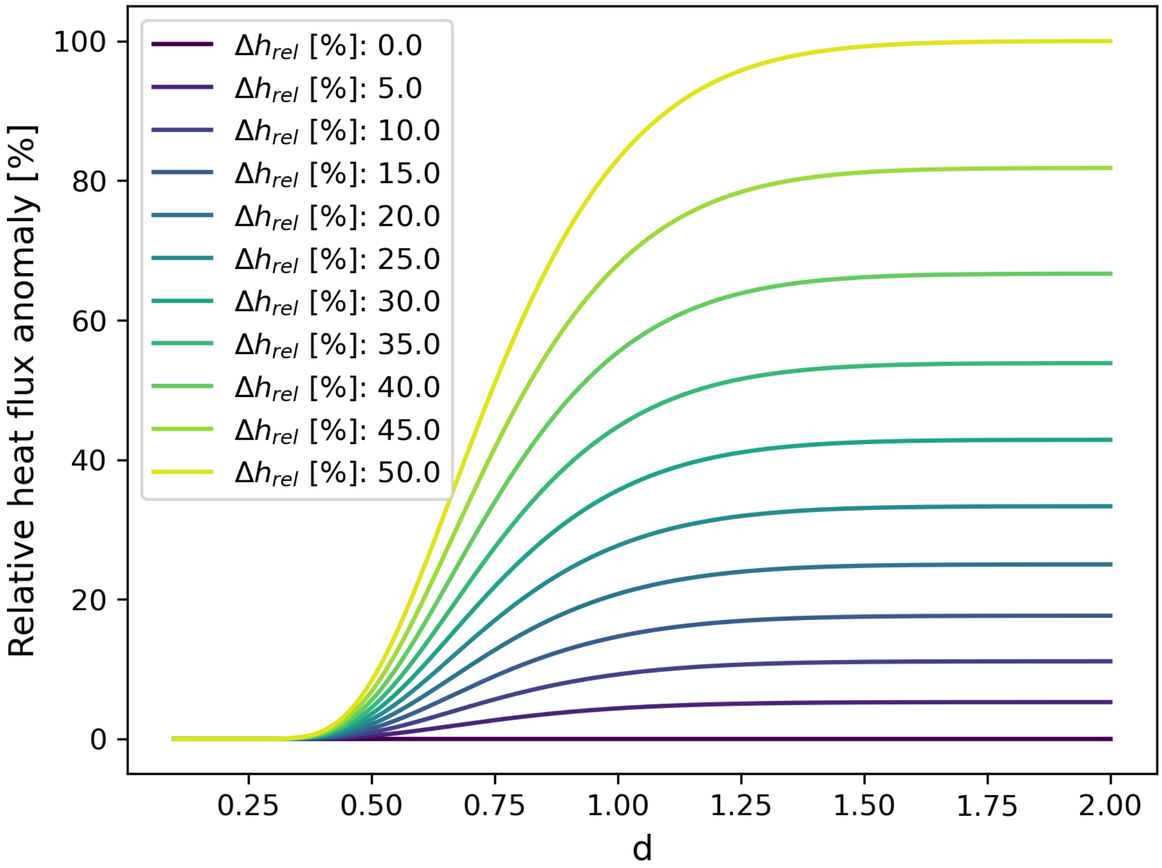

Figure S1. Relative heat flux as a function of d for different values of relative lithosphere thinning Δh_{rel}.

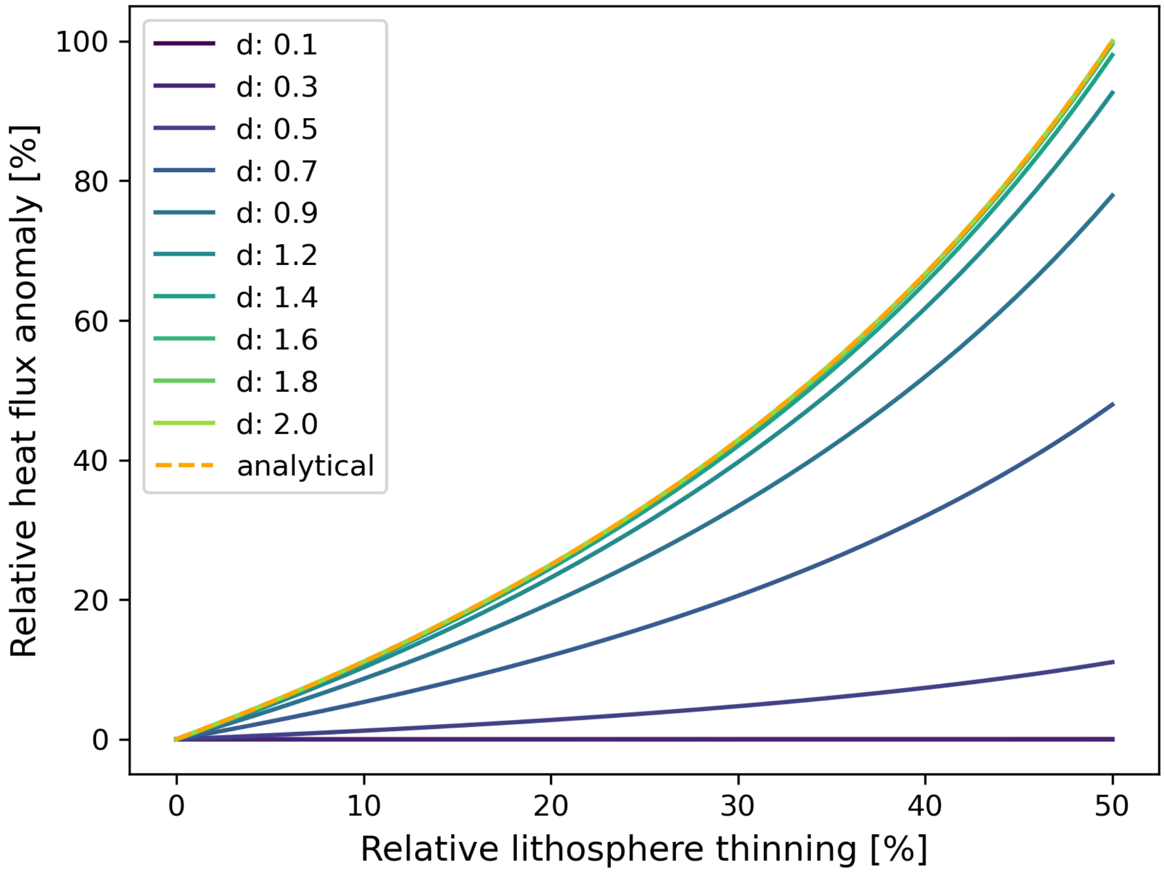

Figure S2. Relative heat flux anomaøy as a function of relative lithosphere thinning Δh_{rel} for different choices of d. The analytical line assumes $d \to \infty$ (see Equation (13)).

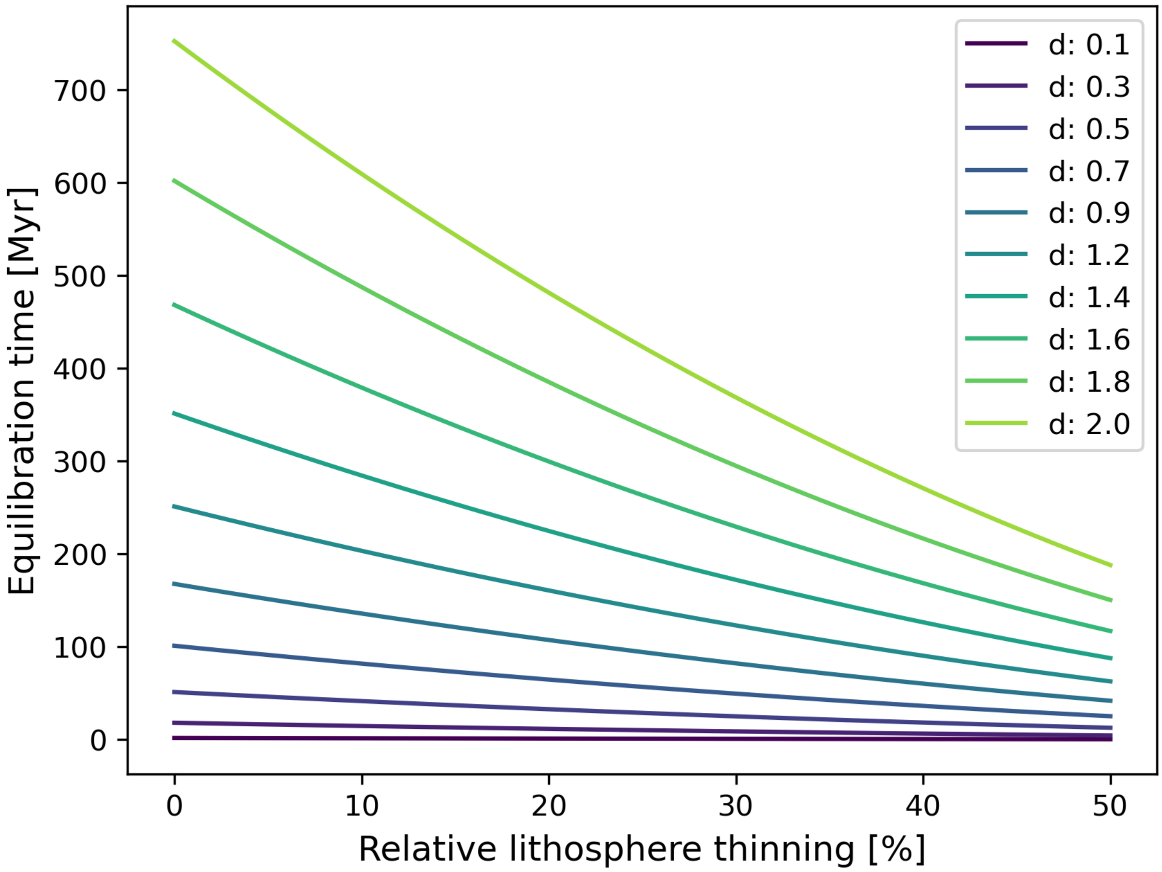

Figure S3. Equivalent equilibration time as a function of relative lithosphere thinning Δh_{rel} for different choices of d and a constant $L = 137.8\,\mathrm{km}$. A value of $d < \infty$, but in practice $d > 2.0$ means that the system does not equilibrate to the maximum heat flux (compare Figure S1). Equilibration is assumed for a stationary model following Equation (11)).

Table S1. Input parameters and their ranges for the numerical models. Only one of the 2-D stagnant plate models has no dedicated low viscosity asthenosphere, otherwise we use a step function at the bottom of the asthenosphere to increase upper mantle viscosity relative to the asthenosphere viscosity. For models with diffusion-dislocation creep, we further set grain size $d = 1 \cdot 10^{-3}$ m, activation energies $E_{\mathrm{diff}} = 373$ kJ/mol and $E_{\mathrm{disl}} = 530$ kJ/mol, activation volumes $V_{\mathrm{diff}} = 6{\cdot}10^{-6}$ m^3/mol and $V_{\mathrm{disl}} = 1.4{\cdot}10^{-5}$ m^3/mol, grain size exponent $m = 3$, stress exponents $n_{\mathrm{diff}} = 1$ and $n_{\mathrm{disl}} = 3.5$, and viscosity prefactors $A_{\mathrm{diff}} = 1.5 \cdot 10^{15}$ m^3/(Pa·s) and $A_{\mathrm{disl}} = 1.1 \cdot 10^{16}$ (Pa$^{-3.5}$·s^{-1}).

Parameter	Reference value	Range	Unit
Thermal diffusivity κ	$0.8 \cdot 10^{-6}$	–	m^2/s
Reference density	3300	–	kg/m^3
Specific heat capacity c_p	1250	–	J/(kg·K)
Gravitational acceleration g	9.81	–	m/s^2
Viscosity prefactor A	$8 \cdot 10^{-12}$	–	1/Pa·s
Thermal expansivity α	$3.5 \cdot 10^{-5}$	–	1/K
Constant radiogenic heating	$7.58 \cdot 10^{-12}$	–	W/kg
Reference viscosity η_{ref}	$1 \cdot 10^{22}$	–	Pa·s
LAB temperature T_{LAB}	1500	1500 – 1623	K
Layer viscosity scalings η_j	$[5 \cdot 10^{22}, 1 \cdot 10^{24}]$	$[1 \cdot 10^{21} - 5 \cdot 10^{23}, 1 \cdot 10^{24}]$	Pa·s
Initial lithosphere thickness L	150	100 – 200	km
Asthenosphere thickness d_{Asth}	150	0 – 200	km
Asthenosphere viscosity η_{Asth}	$1 \cdot 10^{19}$	$5 \cdot 10^{17} - 1 \cdot 10^{20}$	Pa·s
Plume excess temperature T_p	250	100 – 450	K
Maximum lithosphere viscosity η_{max}	$1 \cdot 10^{29}$	$1 \cdot 10^{26} - 1 \cdot 10^{29}$	Pa·s
Plume life time t_p	200	50 – 200	Myr
Plate velocity v	1.5	0.75 – 3.0	cm/yr
Activation energy E	250	100 – 300	kJ/mol

Table S2. Overview of 2-D stagnant plate models used to create the data in Figure 4. The first column defines which parameter(s) defined in Table S1 deviate from the reference values given in Table S1. The other columns are the maximum heat flux anomaly Δq (in mW/m^2), the maximum lithospheric thinning Δh (in km), the reference heat flux q_0 at the time of maximum heat flux (in mW/m^2), and the reference lithosphere thickness L at the time of maxiumum thinning (in km).

Changed parameter(s)	Δq	Δh	q_0	L
– (ref. case)	7.302	51.5	26.685	158.49
$t_p = 100\,\mathrm{Myr}$	4.016	40.6	24.909	175.98
$t_p = 50\,\mathrm{Myr}$	3.223	43.9	24.601	189.58
$T_p = 150\,\mathrm{K}$	5.680	53.1	25.122	173.84
$T_p = 200\,\mathrm{K}$	6.526	53.3	25.899	166.64
$T_p = 300\,\mathrm{K}$	8.097	49.2	27.459	150.97
$T_p = 400\,\mathrm{K}$	10.725	46.9	29.262	136.77
$d_{\mathrm{Asth}} = 0\,\mathrm{km}$	1.349	23.2	23.526	185.92
$d_{\mathrm{Asth}} = 100\,\mathrm{km}$	7.976	54.7	26.269	161.37
$d_{\mathrm{Asth}} = 100\,\mathrm{km},\ t_p = 100\,\mathrm{Myr}$	4.150	41.8	26.521	161.83
$d_{\mathrm{Asth}} = 100\,\mathrm{km},\ t_p = 50\,\mathrm{Myr}$	2.927	39.9	24.588	190.71
$L = 100\,\mathrm{km}$	9.231	47.8	31.059	139.50
$L = 100\,\mathrm{km},\ t_p = 100\,\mathrm{Myr}$	4.745	34.9	33.531	166.96
$L = 100\,\mathrm{km},\ t_p = 50\,\mathrm{Myr}$	2.890	33.1	27.104	173.92
$L = 200\,\mathrm{km}$	5.559	57.2	22.670	186.14
$L = 200\,\mathrm{km},\ t_p = 100\,\mathrm{Myr}$	3.449	48.6	22.238	200.71
$L = 200\,\mathrm{km},\ t_p = 50\,\mathrm{Myr}$	2.741	50.5	21.953	207.58
$E = 100\,\mathrm{kJ/mol}$	43.664	130.4	73.077	223.91
$E = 100\,\mathrm{kJ/mol},\ t_p = 100\,\mathrm{Myr}$	33.518	130.4	61.354	223.91
$E = 150\,\mathrm{kJ/mol}$	25.209	36.9	45.511	99.35
$E = 150\,\mathrm{kJ/mol},\ t_p = 100\,\mathrm{Myr}$	16.665	43.5	36.711	115.60
$E = 200\,\mathrm{kJ/mol}$	18.160	50.3	31.614	122.64
$E = 200\,\mathrm{kJ/mol},\ t_p = 100\,\mathrm{Myr}$	11.355	51.7	29.117	144.90
$\eta_j = [5 \cdot 10^{21}, 1 \cdot 10^{24}]\,\mathrm{Pa{\cdot}s}$	16.314	49.6	31.179	125.72
$\eta_j = [5 \cdot 10^{23}, 1 \cdot 10^{24}]\,\mathrm{Pa{\cdot}s}$	2.159	31.5	24.177	180.62
$\eta_j = [5 \cdot 10^{23}, 1 \cdot 10^{24}]\,\mathrm{Pa{\cdot}s},\ L = 100\,\mathrm{km}$	2.600	27.3	27.629	157.31
$\eta_j = [5{\cdot}10^{23}, 1{\cdot}10^{24}]\,\mathrm{Pa{\cdot}s},\ L = 100\,\mathrm{km},\ \eta_{\max} = 1{\cdot}10^{26}\,\mathrm{Pa{\cdot}s}$	2.601	27.3	27.616	157.32
$\eta_{\max} = 1 \cdot 10^{26}\,\mathrm{Pa{\cdot}s}$	7.345	52.2	26.638	159.14
$\eta_{\max} = 1 \cdot 10^{26}\,\mathrm{Pa{\cdot}s},\ t_p = 100\,\mathrm{Myr}$	4.022	40.8	24.910	176.11
$\eta_{\max} = 1 \cdot 10^{26}\,\mathrm{Pa{\cdot}s},\ t_p = 50\,\mathrm{Myr}$	3.231	44.9	24.590	190.58
$\eta_{\max} = 1 \cdot 10^{26}\,\mathrm{Pa{\cdot}s},\ L = 100\,\mathrm{km}$	9.250	48.3	31.041	140.24
$\eta_{\max} = 1 \cdot 10^{26}\,\mathrm{Pa{\cdot}s},\ L = 100\,\mathrm{km},\ t_p = 100\,\mathrm{Myr}$	4.735	35.0	33.535	165.41
$\eta_{\max} = 1 \cdot 10^{26}\,\mathrm{Pa{\cdot}s},\ L = 100\,\mathrm{km},\ t_p = 50\,\mathrm{Myr}$	2.890	33.0	27.104	173.92
$\eta_{\max} = 1 \cdot 10^{26}\,\mathrm{Pa{\cdot}s},\ L = 200\,\mathrm{km}$	5.605	57.3	22.662	186.04
diffusion-dislocation creep	31.304	80.8	38.961	160.26
$T_{\mathrm{LAB}} = 1623\,\mathrm{K}$	11.012	46.6	30.077	134.97
$T_{\mathrm{LAB}} = 1623\,\mathrm{K},\ t_p = 100\,\mathrm{Myr}$	5.661	31.6	30.517	132.16
$T_{\mathrm{LAB}} = 1623\,\mathrm{K},\ t_p = 50\,\mathrm{Myr}$	3.435	31.6	27.523	160.48
$T_{\mathrm{LAB}} = 1623\,\mathrm{K},\ T_p = 100\,\mathrm{K}$	6.582	43.8	27.673	153.00
$T_{\mathrm{LAB}} = 1623\,\mathrm{K},\ T_p = 400\,\mathrm{K}$	14.370	40.2	33.396	117.52
$T_{\mathrm{LAB}} = 1623\,\mathrm{K},\ d_{\mathrm{Asth}} = 100\,\mathrm{km}$	12.445	53.1	29.626	139.11
$T_{\mathrm{LAB}} = 1623\,\mathrm{K},\ d_{\mathrm{Asth}} = 200\,\mathrm{km}$	9.533	41.2	30.329	132.70
$T_{\mathrm{LAB}} = 1623\,\mathrm{K},\ L = 100\,\mathrm{km}$	13.282	41.7	35.407	117.32
$T_{\mathrm{LAB}} = 1623\,\mathrm{K},\ L = 200\,\mathrm{km}$	8.279	50.7	25.481	158.14

Table S3. Overview of 2-D moving plate models used as data in Figure 4. Definitions as for Table S2.

Changed param.	Δq	Δh	q_0	L
– (reference case)	0.620	15.90	26.834	156.79
$v = 0.75\,\mathrm{cm/yr}$	0.974	21.13	26.478	164.60
$v = 3.0\,\mathrm{cm/yr}$	0.260	8.25	27.131	154.28
$\eta_j = [1\cdot10^{21}, 1\cdot10^{24}]\,\mathrm{Pa{\cdot}s}$	16.866	59.11	27.662	136.54
$\eta_j = [5\cdot10^{21}, 1\cdot10^{24}]\,\mathrm{Pa{\cdot}s}$	1.821	24.10	28.132	151.42
$\eta_j = [1\cdot10^{21}, 1\cdot10^{24}]\,\mathrm{Pa{\cdot}s}$	1.292	18.84	27.560	151.12
$\eta_j = [5\cdot10^{23}, 1\cdot10^{24}]\,\mathrm{Pa{\cdot}s}$	0.049	8.64	27.011	163.30
$E = 150\,\mathrm{kJ/mol}$	11.099	48.86	27.671	141.28
$E = 150\,\mathrm{kJ/mol}$, $v = 3.0\,\mathrm{cm/yr}$	15.721	33.47	37.081	99.87
$E = 150\,\mathrm{kJ/mol}$, $v = 0.75\,\mathrm{cm/yr}$	15.274	53.13	27.771	135.98
$E = 200\,\mathrm{kJ/mol}$	1.624	28.23	28.207	146.12
$T_p = 400\,\mathrm{K}$	1.170	19.95	26.806	159.50
diffusion-dislocation creep	1.338	27.29	27.121	162.03
$T_{\mathrm{LAB}} = 1623\,\mathrm{K}$	1.209	12.02	29.854	133.87
$T_{\mathrm{LAB}} = 1623\,\mathrm{K}$, $v = 0.75\,\mathrm{cm/yr}$	1.717	14.58	30.126	134.01
$T_{\mathrm{LAB}} = 1623\,\mathrm{K}$, $v = 3.0\,\mathrm{cm/yr}$	1.268	16.45	29.972	140.04
$T_{\mathrm{LAB}} = 1623\,\mathrm{K}$, diffusion-dislocation creep	1.650	18.94	31.002	128.98
$T_{\mathrm{LAB}} = 1623\,\mathrm{K}$, $\eta_j = [5\cdot10^{21}, 1\cdot10^{24}]\,\mathrm{Pa{\cdot}s}$	20.114	54.28	30.367	122.63
$T_{\mathrm{LAB}} = 1623\,\mathrm{K}$, $\eta_j = [5\cdot10^{21}, 1\cdot10^{24}]\,\mathrm{Pa{\cdot}s}$,$v = 3.0\,\mathrm{cm/yr}$	12.386	41.60	30.202	124.5
$T_{\mathrm{LAB}} = 1623\,\mathrm{K}$, $\eta_j = [5\cdot10^{21}, 1\cdot10^{24}]\,\mathrm{Pa{\cdot}s}$,$v = 0.75\,\mathrm{cm/yr}$	23.189	55.62	30.532	119.60
$T_{\mathrm{LAB}} = 1623\,\mathrm{K}$, $T_p = 300\,\mathrm{K}$	1.171	12.94	30.515	132.83
$T_{\mathrm{LAB}} = 1623\,\mathrm{K}$, $T_p = 350\,\mathrm{K}$	1.673	14.41	30.069	133.95
$T_{\mathrm{LAB}} = 1623\,\mathrm{K}$, $T_p = 400\,\mathrm{K}$	1.926	16.32	30.276	133.39
$T_{\mathrm{LAB}} = 1623\,\mathrm{K}$, $T_p = 450\,\mathrm{K}$	2.543	18.42	29.741	134.92
$T_{\mathrm{LAB}} = 1623\,\mathrm{K}$, $T_p = 300\,\mathrm{K}$, $v = 0.75\,\mathrm{cm/yr}$	2.283	16.98	29.716	136.93
$T_{\mathrm{LAB}} = 1623\,\mathrm{K}$, $T_p = 300\,\mathrm{K}$, $v = 3.0\,\mathrm{cm/yr}$	1.301	16.66	30.101	137.15
$T_{\mathrm{LAB}} = 1623\,\mathrm{K}$, $T_p = 400\,\mathrm{K}$, $v = 0.75\,\mathrm{cm/yr}$	3.056	22.30	29.833	138.57
$T_{\mathrm{LAB}} = 1623\,\mathrm{K}$, $T_p = 400\,\mathrm{K}$, $v = 3.0\,\mathrm{cm/yr}$	1.555	14.72	30.396	136.39

Table S4. Overview of 3-D moving plate models used as data in Figure 4. Definitions as for Table S2.

Changed param.	Δq	Δh	q_0	L
– (reference case)	1.983	30.21	26.761	161.11
$v = 0.75\,\mathrm{cm/yr}$	4.192	49.55	26.198	170.12
$v = 3.0\,\mathrm{cm/yr}$	0.761	18.23	27.609	153.73
$d_{\mathrm{Asth}} = 100\,\mathrm{km}$	1.248	21.00	27.012	158.34
$T_p = 150\,\mathrm{K}$	0.945	21.00	26.727	161.00
$T_p = 400\,\mathrm{K}$	5.284	50.93	26.753	163.39
$\eta_j = [5\cdot10^{21}, 1\cdot10^{24}]\,\mathrm{Pa{\cdot}s}$	3.446	34.70	28.583	148.52
$\eta_j = [5\cdot10^{23}, 1\cdot10^{24}]\,\mathrm{Pa{\cdot}s}$	0.275	9.75	26.685	162.65
$E = 150\,\mathrm{kJ/mol}$	8.148	48.91	31.198	143.04
$E = 200\,\mathrm{kJ/mol}$	4.566	40.95	28.481	148.76
$E = 300\,\mathrm{kJ/mol}$	0.333	12.03	26.449	165.58